

A mechanistic model for creep and thermal aging in Alloy 709

Applied Materials Division

About Argonne National Laboratory

Argonne is a U.S. Department of Energy laboratory managed by UChicago Argonne, LLC under contract DE-AC02-06CH11357. The Laboratory's main facility is outside Chicago, at 9700 South Cass Avenue, Argonne, Illinois 60439. For information about Argonne and its pioneering science and technology programs, see www.anl.gov.

DOCUMENT AVAILABILITY

Online Access: U.S. Department of Energy (DOE) reports produced after 1991 and a growing number of pre-1991 documents are available free at OSTI.GOV (<http://www.osti.gov/>), a service of the U.S. Dept. of Energy's Office of Scientific and Technical Information

Reports not in digital format may be purchased by the public from the National Technical Information Service (NTIS):

U.S. Department of Commerce
National Technical Information Service
5301 Shawnee Rd
Alexandria, VA 22312
www.ntis.gov
Phone: (800) 553-NTIS (6847) or (703) 605-6000
Fax: (703) 605-6900
Email: orders@ntis.gov

Reports not in digital format are available to DOE and DOE contractors from the Office of Scientific and Technical Information (OSTI)

U.S. Department of Energy
Office of Scientific and Technical Information
P.O. Box 62
Oak Ridge, TN 37831-0062
www.osti.gov
Phone: (865) 576-8401
Fax: (865) 576-5728
Email: reports@osti.gov

Disclaimer

This report was prepared as an account of work sponsored by an agency of the United States Government. Neither the United States Government nor any agency thereof, nor UChicago Argonne, LLC, nor any of their employees or officers, makes any warranty, express or implied, or assumes any legal liability or responsibility for the accuracy, completeness, or usefulness of any information, apparatus, product, or process disclosed, or represents that its use would not infringe privately owned rights. Reference herein to any specific commercial product, process, or service by trade name, trademark, manufacturer, or otherwise, does not necessarily constitute or imply its endorsement, recommendation, or favoring by the United States Government or any agency thereof. The views and opinions of document authors expressed herein do not necessarily state or reflect those of the United States Government or any agency thereof, Argonne National Laboratory, or UChicago Argonne, LLC.

A mechanistic model for creep and thermal aging in Alloy 709

prepared by

Tianchen Hu, Argonne National Laboratory

Hing Ho Janzen Choi, Argonne National Laboratory

Mark C. Messner, Argonne National Laboratory

Applied Materials Division

September 2023

Abstract

This report describes a physics-based model for creep and thermal aging in Alloy 709. Alloy 709 is an advanced austenitic alloy, targeted for use in future Sodium Fast Reactors (SFRs) and other advanced reactors. The material has superior high temperature properties compared to currently qualified 316 and 304 stainless steels. However, the available creep and thermal aging test database for Alloy 709 is significantly more limited compared to the historical materials. The physics-based model developed here is one way to accelerate the qualification of the material by providing more accurate long-term predictions for creep properties and thermal aging, compared to current empirical time-extrapolate techniques. The crystal plasticity finite element model is used to predict the deformation and failure of alloy 709. The same setup for the CPFE model is used in both the baseline model calibration process and the simulation campaigns for parameter inference. Specific constitutive choices are made for Alloy 709 to capture the primary deformation mechanisms. The dislocation creep formulation developed by Hu and Cocks is extended to account for coupled precipitation formation and the grain boundary cavitation model developed by Sham, Needleman, et al. is used to model grain boundary cavitation-induced failure. A novel update algorithm is proposed to render the semi-discrete constitutive update for the Sham-Needleman model unconditionally stable. A progressive calibration approach is adopted based on the observations that several types of material responses can be effectively decoupled. A surrogate model is trained based on full-fledged CPFE simulations to accelerate the forward model evaluations, and stochastic variational inference (SVI) is used to calibrate the unknown microstructural model parameters. The calibrated mechanistic model is used to predict the long-term creep life of Alloy 709, and the predictions are compared against classical empirical approaches.

Table of Contents

Abstract	i
Table of Contents	iii
List of Figures	v
List of Tables	vii
1 Introduction	1
2 Crystal plasticity finite element model setup	3
2.1 Microstructure segmentation and realization	3
2.2 The initial boundary value problem	5
3 Physics-based creep and creep rupture modeling	7
3.1 State-of-the-art dislocation creep formulation	7
3.2 Precipitation competition in Alloy 709 stainless steel	9
3.3 Grain boundary cavitation	10
4 Baseline model calibration	15
4.1 Calibration of short-term creep responses	17
4.2 Calibration of thermal aging effects	20
4.3 Preliminary calibration of the grain boundary cavitation model	22
5 Inference for the remaining parameters	27
5.1 Simulation campaign setup	27
5.2 Surrogate modeling	28
5.3 Statistical inference	29
6 Long-term predictions	33
6.1 The calibrated constitutive model for Alloy 709	33
6.2 Predictions of long-term creep rupture	33
6.3 Summary and future work	36
Bibliography	41

List of Figures

2.1	Characteristics of the raw 709 SEM.	3
2.2	Characteristics of the 709 SEM after segmentation.	3
2.3	Convergence of microstructure reconstruction.	4
2.4	RVE realizations colored by grain IDs.	4
4.1	Stress-strain curves of the high-temperature uniaxial tension tests.	16
4.2	The test conditions of the creep tests.	16
4.3	The calibrated Kocks-Mecking relationship.	21
4.4	Test plan for the expedition CPFE simulation campaign.	23
4.5	(a) Total strain and (b) strain rate as functions of time from the expedition CPFE simulations. The simulated curves are plotted as solid lines, and the experimental curves are plotted as dashed lines. The curves are colored using the pseudo Kocks-Mecking normalization.	24
4.6	The time-to-tertiary predictions using the fitted grain boundary cavitation parameters.	25
5.1	Test plan for the full-fledged CPFE simulation campaign.	27
5.2	Grain boundary cavitation parameters used in the full-fledged CPFE simulation campaign.	28
5.3	Comparison between the surrogate model's time-to-tertiary prediction and the CPFE model's time-to-tertiary prediction.	29
5.4	The grain boundary cavitation parameters inferred by solving (5.3). (left) Cavity diffusivity as a function of temperature. (right) Reference cavity nucleation rate as a function of temperature. Mean values of posterior estimates are plotted as solid black lines. The 90% confidence intervals are indicated using gray shadow.	30
5.5	The posterior estimates of time-to-rupture t_r predictions at different temperatures. Experimental observations are marked as dots. Mean predictions are plotted as solid lines. The 90% confidence intervals are indicated using light shadows of the same color. All points are color-coded based on the temperature.	31
6.1	The fitted Larson-Miller time-temperature parameters as functions of rupture stress.	35
6.2	Time-to-rupture predictions by (a) the physics-based mechanistic model, (b) the linear Larson-Miller correlation, and (c) the quadratic Larson-Miller correlation. Points are color-coded using the temperature. 90% confidence intervals are shaded.	35

List of Tables

3.1	Major stable phases and their compositions.	9
4.1	Summary of material properties and model parameters.	17
4.2	Summary of material properties and model parameters for the carbide phase.	18
4.3	Summary of material properties and model parameters for the Laves phase.	18
4.4	Summary of material properties and model parameters for the nitride phase.	18
4.5	Summary of calibrated parameters that control the short-term responses.	20
4.6	Summary of calibrated parameters that control the thermal aging effects.	22
4.7	Summary of the initial calibration of grain boundary cavitation parameters.	24
6.1	Summary of calibrated material properties and model parameters.	33
6.2	Summary of calibrated parameters that control the short-term responses.	33
6.3	Summary of calibrated parameters that control the thermal aging effects.	34
6.4	Summary of the calibrated grain boundary cavitation parameters.	34
6.5	Rupture strength (MPa) predictions at 700K	35
6.6	Rupture strength (MPa) predictions at 800K	36
6.7	Rupture strength (MPa) predictions at 900K	36

1 Introduction

This report documents the development of a physics-based mechanistic model for predicting creep and thermal aging in Alloy 709. The basic framework was developed through the DOE:NE NMDQi program, [3] where the creep of type 316H stainless steel was successfully modeled. That work demonstrated the predictions made by the mechanistic model are more accurate than the classical purely data-driven approaches (e.g., Larson-Miller [13]).

Alloy 709 is an advanced austenitic stainless steel, targeted for use in future Sodium Fast Reactors (SFRs) and other advanced reactors. Alloy 709 has better high temperature creep strength compared to the currently-qualified 316H stainless steel while having comparable thermal and environmental properties. Qualifying Alloy 709 for use in future advanced reactors could have significant economic benefits by improving the safety and reliability of future reactors.

However, the available database of long-term tests for Alloy 709 is much smaller compared to 316H and other currently-qualified historical materials. Reliably determining long-term creep and thermal aging properties for a material is critical for qualifying it for use in high temperature nuclear reactors. Applying the physics-based model to predict long-term creep and aging in Alloy 709 could provide more reliable long-term predictions for these key material properties, reducing the need for long-duration tests and accelerating the qualification and application of the material.

The project is a collaboration between the DOE:NE NEAMS program, providing the modeling and simulation development and the application to Alloy 709 described in this report, and the DOE:NE ART program, which is tasked with qualifying the material and provided the experimental data used here.

The key challenge for Alloy 709 compared to past work on 316H is that we do not have long-term test data available to directly validate the model predictions. Here we compare the results of the physics-based model to conventional time-temperature parameter extrapolation to elucidate the differences in long-term predictions.

Most codes and standards allow some limited extrapolation in time outside the direct test data using a time-temperature parameter [13, 15, 16] to trade higher temperature testing for shorter test times. For example, the ASME Boiler & Pressure Vessel Code Section III, Division 5 rules covering the design and construction of high temperature reactor structural components limits the allowed extrapolation to a factor of 3 to 5 in time, as described in Section III, Division 5, Subsection HB, Subpart B, Appendix HBB-Y. Many reactor designs call for 30 or even 60 year initial design lives in order to amortize plant capital costs. Given these targets, a minimum full-life qualification program would require creep rupture testing with times from 6 to 20 years before a new material could be entered into service.

The physics-based approach was proposed in [3] aiming at extending the extrapolation window to reduce the number and duration of creep tests required to qualify a material for a 30 to 60 year life. This model uses the crystal plasticity finite element (CPFE) method to discretize the microstructure of the material and capture key aspects of the material structure. A single crystal model captures the details of grain bulk deformation, linking bulk creep to the underlying physical mechanisms of dislocation motion, precipitate hardening, solid solution strengthening, and bulk vacancy diffusion causing the deformation. The model also includes a grain boundary cavitation model [5] to represent grain boundary sliding and diffusion assisted creep-cavitation and eventual grain boundary failure.

This report documents the application of the physics-based approach to model creep and thermal aging in Alloy 709. Chapter 2 describes the microstructure generation and the CPFE simulation setup. Chapter 3 describes the special constitutive choices made for Alloy 709. Chapter 4 and 5 outline the procedure for calibrating and inferring various material properties and model parameters. The report is concluded in Chapter 6 by comparing the physics-based predictions against classical data-driven approaches.

2 Crystal plasticity finite element model setup

This chapter presents the crystal plasticity finite element (CPFE) model used to predict the deformation and failure of Alloy 709. The same setup for the CPFE model is used in both the baseline model calibration process (Chapter 4) and the simulation campaigns for parameter inference (Chapter 5).

In essence, the CPFE model solves equilibrium on a representative volume element (RVE) under periodic boundary conditions. The realization of microstructures is described in Section 2.1, and the initial boundary value problem (IBVP) that governs the balance of linear momentum is summarized in Section 2.2.

2.1 Microstructure segmentation and realization

The RVE used in the CPFE simulation consists of multiple grains with different grain orientations. A scanning electron microscopy (SEM) image of a Alloy 709 sample (Figure 2.1) is produced to extract realistic grain sizes and orientation distributions.

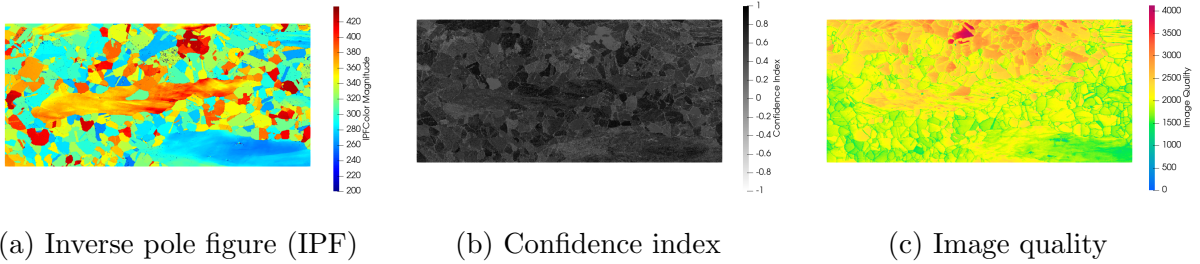


Figure 2.1: Characteristics of the raw 709 SEM.

First, the SEM image is segmented to identify individual grains using DREAM.3D. Voxels with confidence index below 0.1 and image quality below 120 are marked as bad voxels; bad voxels are correlated with neighbor voxels if the misorientation is below 5° ; contiguous voxels with misorientation below 5° are segmented into the same grain; neighboring grains that are in a twin relationship are merged; isolated grains with size smaller than 128 voxels or with fewer than 4 neighbors are removed, eroded and dilated by neighbor coarsening. The post-segmentation microstructure is shown in Figure 2.2.

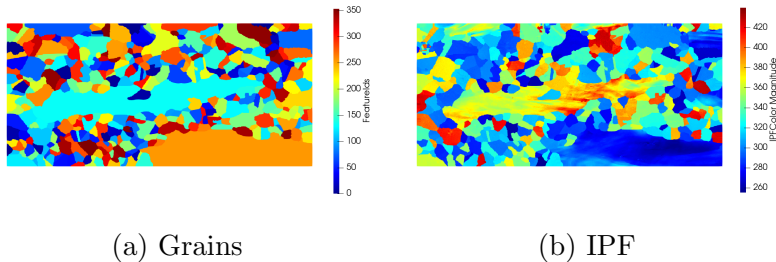


Figure 2.2: Characteristics of the 709 SEM after segmentation.

Next, grain-specific characteristics are extracted from the post-segmentation image. The list of data include: centroids, equivalent diameters, volumes, and neighborhoods. In addi-

tion, each grain is fitted using a ellipsoid to approximate the principal axis lengths, principal axis directions, aspect ratios, and (second-order rotational) moment invariants. Crystallographic statistics are then computed based on the extracted data. In particular, log-normal distributions are fitted against the equivalent diameters and the neighborhoods, and beta distributions are fitted against the aspect ratios and the moment invariants. RVEs can be reconstructed using the fitted distributions. Convergence of the reconstruction with respect to number of sampled grains is plotted in Figure 2.3.

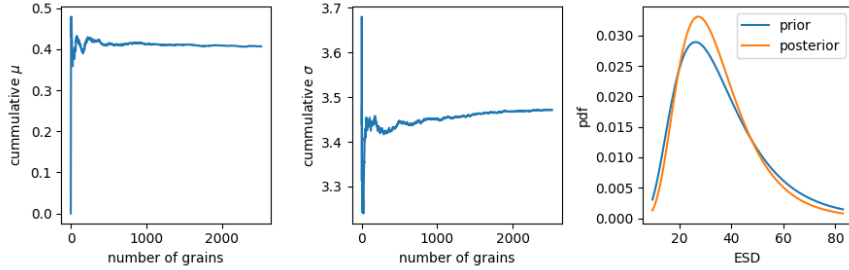


Figure 2.3: Cumulative mean (left) and standard deviation (middle) of the equivalent spherical diameter (ESD) of the sampled grains. (right) Comparison between the target (prior) ESD distribution and the realized (posterior) ESD distribution.

As shown in Figure 2.3, a reasonable convergence is obtained with approximately 300 grains. Therefore, 10 realizations of the microstructure, each with approximately 30 grains, are reconstructed from the fitted distributions as the RVEs for the CPFE simulations. The microstructures are meshed with 8-noded hexahedrons using Sculpt, a parallel all-hex meshing tool developed by the Sandia National Laboratories. The discretized RVE realizations are shown in Figure 2.4. These discretizations serve as the basis for the CPFE IBVP detailed in Section 2.2.

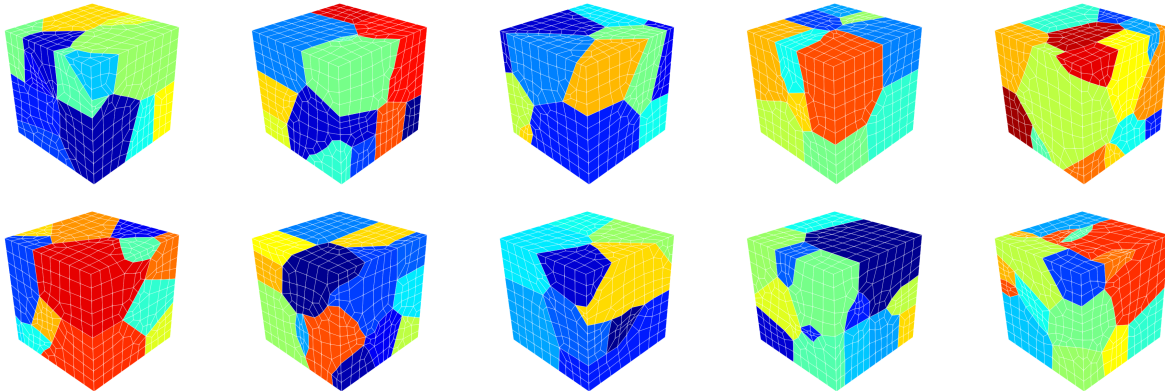


Figure 2.4: RVE realizations colored by grain IDs using a linear RGB color mapping ranging from 1 to 30. Hexahedron element edges are colored in white.

2.2 The initial boundary value problem

Consider the RVE domain Ω , with disjointly partitioned Dirichlet and Neumann boundaries $\partial_D\Omega$ and $\partial_N\Omega$, i.e. $\partial_D\Omega \cup \partial_N\Omega = \partial\Omega$, as well as grain boundaries Γ defined as the interfaces between grains. The deformation is characterized by the deformation map φ , with $\mathbf{x} = \varphi(\mathbf{X})$ where \mathbf{x} belongs to the current configuration and \mathbf{X} belongs to the reference (undeformed) configuration, and the displacement $\mathbf{u} := \mathbf{x} - \mathbf{X}$. The balance of linear momentum (neglecting body force) can be stated as

$$\nabla \cdot \boldsymbol{\sigma} = 0, \quad \text{in } \Omega, \quad (2.1a)$$

$$[\![\mathbf{t}]\!] = \mathbf{0}, \quad \text{on } \Gamma, \quad (2.1b)$$

$$\boldsymbol{\sigma} \cdot \mathbf{n} = \mathbf{t}_g, \quad \text{on } \partial_N\Omega, \quad (2.1c)$$

$$\mathbf{u} = \mathbf{u}_g, \quad \text{on } \partial_D\Omega, \quad (2.1d)$$

where $\boldsymbol{\sigma}$ is the Cauchy stress, \mathbf{t} is the interface traction, and \mathbf{u}_g is the prescribed displacement. Together with the appropriate initial conditions for the constitutive models, (2.1) forms the IBVP to be solved in the CPFE simulations.

- To model uniaxial creep, a traction boundary condition $\mathbf{t} \cdot \mathbf{n} = t_g$ is applied at the right side ($\mathbf{n} \cdot \mathbf{e}_x = 1$) with a linear ramp-up time of 0.1h. The applied traction is held constant after the ramp-up.
- To approximate periodicity, Dirichlet boundary conditions $\mathbf{u} \cdot \mathbf{n} = 0$ are applied at the left side ($\mathbf{n} \cdot \mathbf{e}_x = -1$), the bottom side ($\mathbf{n} \cdot \mathbf{e}_y = -1$), and the back side ($\mathbf{n} \cdot \mathbf{e}_z = -1$), and planar displacement constraints $\mathbf{u}_g \cdot \mathbf{n} - \int \mathbf{u}_g \cdot \mathbf{n} \, dA = 0$ are applied at the rest of the sides.
- For thermal aging, isothermal and adiabatic assumptions are made, and so a constant and homogeneous temperature is applied throughout the entire simulation.

The large deformation stress-strain and traction-separation constitutive models are discussed in detail in Chapter 3. The CPFE simulations are set up using blackbear, a MOOSE-based application for structural materials and their degradation developed by the Idaho National Laboratory.

3 Physics-based creep and creep rupture modeling

The CPFE model described in Section 2.2 is generally applicable to any microstructure that can be represented as a continuum solid. The IBVP is partially defined up to the material-specific constitutive models including the large deformation stress-strain relation and the large deformation traction-separation law. In this chapter, specific constitutive models for alloy 709 are presented. These models are constructed and developed to capture the primary deformation mechanisms in this alloy. First, a dislocation creep formulation developed by Hu and Cocks is summarized in Section 3.1. The model is extended in Section 3.2 to account for coupled precipitation formation. A grain boundary cavitation model developed by Sham, Needleman, et al. is summarized in Section 3.3, including a novel update algorithm to render the semi-discrete constitutive update unconditionally stable.

This chapter presents the formulation for the plastic flow rate. The crystal plasticity constitutive update was implemented in NEML, a material modeling library developed at the Argonne National Laboratory. The full mathematical description of the update can be found at [7]. The large deformation traction-separation law is presented in a local orthonormal coordinate system. The global-local transformation and the large kinematics integration have been documented in a previous report [5].

3.1 State-of-the-art dislocation creep formulation

In this work, we use a single crystal, physics-based model for the creep deformation of alloy 709. The model was originally developed by Hu and Cocks et al. in [1] and in Hu's dissertation [2] to model type 316H stainless steel. The model has been implemented in the MOOSE-based CPFE framework in a previous work [3] which has been successfully applied to model the long-term creep rupture of 316H stainless steel. The current version of the creep model is summarized below for convenience. The complete description of the model and its implementation can be found in the aforementioned references.

The model developed by Hu and Cocks et al. for 316H (hereinafter referred to as the Hu-Cocks model) considers three strengthening mechanisms¹: dislocation forest hardening, precipitation hardening, and solid solution hardening. The plastic flow rate $\dot{\gamma}_i$ for the i -th

¹The full model additionally includes mechanisms for dislocation pileups and solute drag. These mechanisms are neglected in the implementation in [3] based on sensitivity analysis.

slip system ($i \in \mathbb{N}$) follows a power law

$$\dot{\gamma}_i = \dot{\gamma}_0 \left| \frac{\tau_i}{\tau_{c,i}} \right|^n \operatorname{sgn}(\tau_i), \quad (3.1a)$$

$$\tau_{c,i} = \sqrt{\tau_{d,i}^2 + \tau_p^2} + \tau_s, \quad (3.1b)$$

$$\tau_{d,i} = \frac{\alpha_d G b}{L_{d,i}}, \quad (3.1c)$$

$$\tau_p = \alpha_p G b \sqrt{\sum_i r_i N_i}, \quad (3.1d)$$

$$\tau_s = \alpha_s G b \sqrt{b \sum_j \frac{c_j}{\omega}}, \quad (3.1e)$$

where $\dot{\gamma}_0$ is the reference flow rate, τ_i is the shear stress resolved on the i -th slip system, $\tau_{c,i}$ is the critical resolved shear stress (CRSS) on the i -th slip system, and n is the power-law exponent. The CRSS is collectively determined by the three deformation mechanisms: The dislocation hardening increases as the dislocation spacing decreases, the precipitation hardening is proportional to the amount of precipitate, and the solid solution strength scales with the amount of solute. α_d , α_p , and α_s are the interaction coefficients for the corresponding mechanisms. The current state of hardening is characterized by three types internal state variables

- the dislocation spacing for the i -th slip system $L_{d,i}$,
- the average radius of the i -th precipitate r_i , and
- the number density of the i -th precipitate N_i .

The dislocation hardening accounts for both self- and latent-forest hardening, i.e.

$$\dot{L}_{d,i} = -L_{d,i}^3 \left(J_1 |\dot{\gamma}_i| + J_2 \sum_{i \neq j} |\dot{\gamma}_i| \right) + \frac{K_0}{L_{d,i}^3} \exp \left(-\frac{Q_K}{RT} \right), \quad (3.2)$$

with J_1 the self-hardening coefficient, J_2 the latent-hardening coefficient, K_0 the reference static recovery coefficient, Q_K the activation energy for static recovery, R the ideal gas constant, and T the temperature in Kelvin.

The nucleation and the growth of the precipitates can be divided into two regimes: the growth regime, followed by the ripening regime. The volume fraction of the precipitate increases in the growth regime and remains the same in the ripening regime. In the growth regime, nucleation and growth are given as

$$\dot{r} = \frac{D_0}{r} \frac{c - c^*}{c_p - c^*} \exp \left(-\frac{Q_D}{RT} \right) - \frac{\dot{N}}{N} \left(\frac{2\chi}{\mathcal{G}} + r \right), \quad (3.3a)$$

$$\dot{N} = N_0 \frac{2\omega D_0 c}{a_m^4} \sqrt{\frac{\chi}{kT}} \exp \left(-\frac{Q_D}{RT} \right) \exp \left(-\frac{16\pi\chi^3}{3\mathcal{G}^2 kT} \right) \quad (3.3b)$$

with D_0 the reference diffusivity, c the concentration of the chemical species², c^* the equilibrium concentration, c_p the concentration in the precipitate, χ the interface energy, \mathcal{G} the Gibbs free energy driving the precipitation, N_0 the reference nucleation rate, ω the molar volume of the precipitate, a_m the lattice parameter, and k the Boltzmann constant. In the ripening regime, the precipitate ripens, and the number density is governed by the geometric relation, i.e.,

$$\dot{r} = \frac{8}{9} \frac{C_f \chi N_a \omega D c}{R T}, \quad (3.4a)$$

$$\dot{N} = -3N \frac{\dot{r}}{r}, \quad (3.4b)$$

where C_f is the coarsening factor, and N_a is the Avogadro's number.

3.2 Precipitation competition in Alloy 709 stainless steel

The original Hu-Cocks model presented in Section 3.1 was developed under the major assumption that different precipitates do not compete for the same chemical species. This assumption has been justified in the previous study on 316H stainless steel [3], where the concentration of molybdenum (Mo) for the Laves phase and the concentrations of carbon (C) and chromium (Cr) for the carbides are tracked.

To validate such assumption, stable phases are calculated using **ThermoCalc** (version 2022b) database TCFE9: Steels/Fe-Alloys (v9.3). Major stable phases and their compositions are summarized in Table 3.1.

Table 3.1: Major stable phases and their compositions in Alloy 709 based on **ThermoCalc** calculations. Phases with volume fractions less than 0.01 are considered minor. Chemical species with mass fraction less than 0.01 are neglected. Chemical species are listed in the order of descending mass fraction in the corresponding phase.

Stable phase	Composition
Nitride	Cr, N, Mo
Carbide	Cr, Mo, Fe, C
Laves ³	Mo, Fe, Cr

According to the **ThermoCalc** calculations, the assumption of independent precipitation no longer holds for Alloy 709 stainless steel. Therefore, the original Hu-Cocks formulation has to be generalized to account for the competition between precipitates for the same chemical species. In particular:

- The definition of the solution concentration should account for the fact that the same chemical species can exist in multiple precipitates;

²Unless explicitly noted by the subscripts/superscripts, the chemical species of interest is the rate-limiting species in the reaction.

³The Laves phase is stable below 700°C

- The Gibbs free energy should account for the coupling between different precipitates;
- The solid solution strengthening should normalize each concentration by the effective molar volume of all the hosting precipitates.

With mass conservation in an arbitrary control volume, the concentration for species j satisfies $\dot{c}_j = 0$. Hence the following relation holds for every species at any point in time:

$$c_{0,j} = \left(1 - \sum_i f_i \mathbb{1}(c_{p,ij}) \right) c_j + \sum_i f_i c_{p,ij}, \quad (3.5)$$

where $c_{0,j}$ is the initial condition for c_j , f_i is the volume fraction of the i -th precipitate, and $c_{p,ij}$ is the concentration of the j -th species in the i -th precipitate. Rearranging (3.5) yields the generalized expression for the solution concentration for the j -th species

$$c_j = \frac{c_{0,j} - \sum_i f_i c_{p,ij}}{1 - \sum_i f_i \mathbb{1}(c_{p,ij})}. \quad (3.6)$$

Similarly, the Gibbs free energy for the i -th precipitate during the precipitation reaction inherits the definition of the coupled solution concentration and is generalized as

$$\mathcal{G}_i = \frac{-kT}{\omega_i} \sum_j \ln \left(\frac{c_j}{c_j^*} \right), \quad (3.7)$$

and the effective molar volume of the precipitate used to measure the solid solution strengthening is defined as

$$\bar{\omega} = \frac{\sum_i f_i \omega_i \mathbb{1}(c_{p,ij})}{\sum_i f_i \mathbb{1}(c_{p,ij})}. \quad (3.8)$$

Remark. Note that in the case of decoupled precipitates, i.e., $c_{p,ij} = 0$ if $i \neq j$, the solution concentration reduces to

$$c_j = \frac{c_{0,j} - \sum_i f_i c_{p,ij} \delta_{ij}}{1 - \sum_i f_i \mathbb{1}(c_{p,ij} \delta_{ij})} = \frac{c_{0,j} - f_j c_{p,j}}{1 - f_j},$$

which is consistent with the original expression from previous studies e.g., [2, 3].

3.3 Grain boundary cavitation

In this work, we use the Sham-Needleman type cavitation model as the traction-separation law on the grain boundaries. A description of the complete formulation can be found in [4]. A preliminary implementation of this model has been documented in the report [5].

In what follows, the model (in its incremental form) is summarized for convenience, and a stable update algorithm is proposed to robustly perform the constitutive update. The cavity nucleation and growth are characterized by two internal variables, the average cavity half spacing b and the average cavity radius a , respectively. Note that the cavity number density N and the average cavity half spacing b are related geometrically via $\pi b^2 N = 1$. Similarly,

the cavity volume V and the cavity radius a are geometrically related as $V = \frac{4}{3}\pi h a^3$ with $h(\psi)$ the geometric shape factor for a spherical cap of angle ψ .

With the backward-Euler time integration scheme, the decrement in the average cavity half spacing (or equivalently the increment in the cavity number density) can be written as

$$\Delta b = -\frac{b}{2} \frac{\Delta N}{N}, \quad (3.9a)$$

$$\Delta N = F_N \left(\frac{\langle T_n \rangle}{\Sigma_0} \right)^\gamma \Delta \bar{\varepsilon} \mathbb{1}(N - N_c), \quad (3.9b)$$

where F_N is the reference cavity nucleation rate, T_n is the normal traction on the grain boundary, Σ_0 is the reference traction, γ is the power-law exponent, $\Delta \bar{\varepsilon}$ is the increment of the equivalent plastic strain, and N_c is the critical number density.

The increment in the average cavity radius (or equivalently the increment in the average cavity volume) can be written as

$$\Delta a = \frac{a}{3} \frac{\Delta V^d + \Delta V^c}{V}, \quad (3.10a)$$

$$\Delta V^d = 8\pi D \frac{T_n}{q} \quad (3.10b)$$

$$\Delta V^c = H(1 - |\eta|) \Delta V^{c,L} + H(|\eta| - 1) \Delta V^{c,H} \quad (3.10c)$$

$$\Delta V^{c,L} = \frac{3}{2} \Delta \bar{\varepsilon} \eta (\alpha + \beta)^n V \quad (3.10d)$$

$$\Delta V^{c,H} = \frac{3}{2} \Delta \bar{\varepsilon} \operatorname{sgn}(\eta) (\alpha \eta + \beta)^n V, \quad (3.10e)$$

where D is the cavity diffusivity, and η is the stress triaxiality. Auxiliary definitions for h , q , α , and β are given below

$$h = \left[\frac{1}{1 + \cos(\psi)} - \frac{\cos(\psi)}{2} \right] \frac{1}{\sin(\psi)} \quad (3.11a)$$

$$q = -2 \ln(f) - (1 - f)(3 - f) \quad (3.11b)$$

$$f = \max \left[\left(\frac{a}{b} \right)^2, \left(\frac{a}{a + 1.5L} \right)^2 \right], \quad L = \left(\frac{D\sigma_{vm}\Delta t}{\Delta \bar{\varepsilon}} \right)^{1/3} \quad (3.11c)$$

$$\alpha = \frac{3}{2n}, \quad \beta = \frac{(n - 1)(n + g)}{n^2} \quad (3.11d)$$

with n the power-law creep exponent in the solid material in the neighborhood of the grain boundary.

The traction-separation law is derived based on the micro-macro split and the active-inactive split of the displacement jump across the grain boundary:

$$[\![\mathbf{u}]\!] = [\![\mathbf{u}]\!]_{\text{active}} + [\![\mathbf{u}]\!]_{\text{inactive}} + [\![\mathbf{u}]\!]^{\text{micro}}, \quad (3.12a)$$

$$[\![\mathbf{u}]\!]_{\text{active}} = \langle [\![\mathbf{u}]\!]_n^{\text{macro}} \rangle_+ \mathbf{e}_n + [\![\mathbf{u}]\!]_t^{\text{macro}} \mathbf{e}_t + [\![\mathbf{u}]\!]_s^{\text{macro}} \mathbf{e}_s, \quad (3.12b)$$

$$[\![\mathbf{u}]\!]_{\text{inactive}}^{\text{macro}} = \langle [\![\mathbf{u}]\!]_n^{\text{macro}} \rangle_- \mathbf{e}_n, \quad (3.12c)$$

$$[\![\mathbf{u}]\!]_n^{\text{micro}} = \frac{V}{\pi b^2}, \quad [\![\mathbf{u}]\!]_t^{\text{micro}} = [\![\mathbf{u}]\!]_s^{\text{micro}} = 0. \quad (3.12d)$$

The traction-separation law is linear elastic followed by damage softening:

$$\mathbf{t} = \left[1 - \left(\frac{a}{b} \right)^m \right] \mathbf{C}[\mathbf{u}]_{\text{active}}^{\text{macro}} + \mathbf{C}[\mathbf{u}]_{\text{inactive}}^{\text{macro}}, \quad (3.13a)$$

$$\mathbf{C} = C_{nn} \mathbf{e}_n \otimes \mathbf{e}_n + C_{tt} \mathbf{e}_t \otimes \mathbf{e}_t + C_{ss} \mathbf{e}_s \otimes \mathbf{e}_s, \quad (3.13b)$$

$$C_{nn} = \frac{E}{w} P (1 + \langle -[\mathbf{u}]_n \rangle^2), \quad (3.13c)$$

$$C_{tt} = C_{ss} = \frac{G}{w}, \quad (3.13d)$$

where \mathbf{e}_n , \mathbf{e}_t , and \mathbf{e}_s form the local orthonormal coordinates on the grain boundary, E and G are the normal and shear stiffness, w is the fictitious thickness of the grain boundary, P is the penalty parameter to prevent interpenetration, and m is the damage softening exponent.

The underlying potential of the fully-coupled traction-separation law with damage softening is non-convex. See e.g. [6] for analysis on similar functionals. The nonconvexity leads to numerical instability especially in the softening regime (i.e., after the onset of tertiary creep). Moreover, based on our experience, the triaxiality dependence in the formulation leads to a small basin of traction during the Newton-Raphson iterations, and so limits the time step size in the numerical simulation. These issues prevent the usage of the current grain boundary cavitation model in practical simulation campaigns, where thousands of simulations with different material properties and different boundary conditions need to be carried out.

To solve these issues, we propose a slightly decoupled update strategy in conjunction with the fixed-point iteration strategy to robustly perform the constitutive update. The algorithm is designed based on the observations that

- With fixed average cavity radius a and fixed average cavity half spacing b , the partial potential associated with the traction-separation law is fully convex, as long as both the grain boundary stiffness matrix \mathbf{C} and the deformation gradient \mathbf{F} (in the context of large deformation kinematics) are positive definite, and the damage degradation function is non-concave, i.e., $m \in [0, 1]$.
- With fixed traction, the partial potentials associated with a and b are fully convex, with mild bound constraints. Denote quantities from the previously converged time step with an overhead $\bar{\cdot}$, the gradients of the partial potentials can be written as

$$\begin{aligned} r_a &= \Delta a (\bar{a} + \Delta a)^2 - \frac{\Delta V}{4\pi h}, \\ r_b &= \Delta b + \frac{\pi \Delta N}{2} (\bar{b} + \Delta b)^3, \\ \text{subject to } \Delta a &\geq 0, \quad \Delta b \leq 0, \quad \frac{\bar{a} + \Delta a}{\bar{b} + \Delta b} \leq 1, \end{aligned}$$

which results in a positive definite system. Note that both ΔV and ΔN are constants with fixed traction.

The algorithm for the grain boundary constitutive update is outlined in Algorithm 1. Note that (3.14) can be treated as an implicit system of equations. Alternatively, analytical

formulae can be derived to update a and b owing to their polynomial form (and a unique solution exist owing to their convexity):

$$a = \frac{1}{3} \left(\frac{\bar{a}^2}{c} + \bar{a} + c \right), \quad c = \frac{\sqrt{2}}{2} \sqrt[3]{3\sqrt{12d\bar{a}^3 + 81\bar{d}^2} + 2\bar{a}^3 + 27d}, \quad d = \frac{\Delta V}{4\pi h}, \quad (3.15a)$$

$$b = \frac{p}{\sqrt[3]{18q}} - \frac{\sqrt[3]{2/3}}{p}, \quad p = \sqrt[3]{\sqrt{81q^4\bar{b}^2 + 12q^3} + 9q^2\bar{b}}, \quad q = \frac{\pi}{2}\Delta N. \quad (3.15b)$$

The first two bound constraints are already satisfied with non-negative ΔV and ΔN . The last bound constraint can be satisfied with a simple line search.

Algorithm 1: The fixed-point iteration algorithm for performing the constitutive update using the grain boundary cavitation model.

input : displacement jump $[\mathbf{u}]$

output: traction \mathbf{t} , average cavity radius a , average cavity half spacing b

Assume an elastic step: $a_0 \leftarrow \bar{a}$, $b_0 \leftarrow \bar{b}$;

Perform micro-macro split and active-inactive split (3.12);

Initialize the fixed-point iteration counter: $i \leftarrow 0$;

while not converged **do**

Update counter: $i \leftarrow i + 1$;

Calculate traction \mathbf{t}_i with a_{i-1} and b_{i-1} (3.13);

Calculate the driving force for cavity growth ΔV_i with \mathbf{t}_i (3.10);

Calculate the driving force for cavity nucleation ΔN_i with \mathbf{t}_i (3.11);

Update a_i and b_i with ΔV_i and ΔN_i (3.14);

end

Set $\mathbf{t} \leftarrow \mathbf{t}_i$, $a \leftarrow a_i$, $b \leftarrow b_i$;

Return \mathbf{t} , a , b ;

4 Baseline model calibration

The constitutive models presented in Chapter 3 capture a wide range of deformation mechanisms including:

- rate sensitive plastic flow, caused by dislocation motion,
- dislocation forest hardening,
- static dislocation recovery,
- precipitation hardening,
- solid solution strengthening,
- coupled precipitate nucleation, growth and ripening,
- grain boundary cavity nucleation and growth, and
- irreversible grain boundary softening due to cavitation.

All of these mechanisms have proven to be important based on previous studies on 316H stainless steel and Grade 91 steel [3, 5]. The effects of these mechanisms are controlled by a large number of parameters summarized in Tables 4.1, 4.2, 4.3, and 4.4. The tables are filled with property and parameter values that are available from the literature for the same (or similar) alloy/precipitate/species. Empty cells represent unavailable values without prior calibration. A total of 58 parameters/properties are required for the constitutive models for Alloy 709, 18 of which are unavailable without calibration. Moreover, some microstructural parameters such as the interaction coefficients, the grain boundary cavitation parameters, and the precipitate nucleation rates are difficult to measure. This chapter documents the calibration procedure for the “measurable” properties and parameters, which produces a baseline model for further calibration of microstructural parameters using CPFE simulations and statistical inference (Chapter 5).

A total of 10 high-temperature uniaxial tension tests were carried out by the Argonne National Laboratory. The tension tests are performed at three different temperatures: 550°C, 600°C, and 650°C. 3 out of the 10 tension tests used as-received (“unaged”) alloy 709 specimen. 7 out of the 10 tension tests used thermally aged specimen with different aging durations. The measured stress-strain curves are plotted in Figure 4.1. A total of 77 high-temperature creep tests were carried out, 17 of which were carried out by the Idaho National Laboratory, 29 of which were carried out by the Oak Ridge National Laboratory, and 31 of which were carried out by the Argonne National Laboratory. The test conditions are summarized in Figure 4.2.

A simplistic monolithic calibration approach is to optimize all 18 unknown parameters together by simulating tension tests (of as-received specimen and of thermally-aged specimen) and creep tests together. Such approach is challenging because

- The parameter space grows exponentially with the number of parameters; with 18 parameters, the parameter space is too large to be practically tractable.
- Calibrating the grain boundary cavitation parameters requires full-fledged CPFE simulations, which makes each objective evaluation computationally expensive.

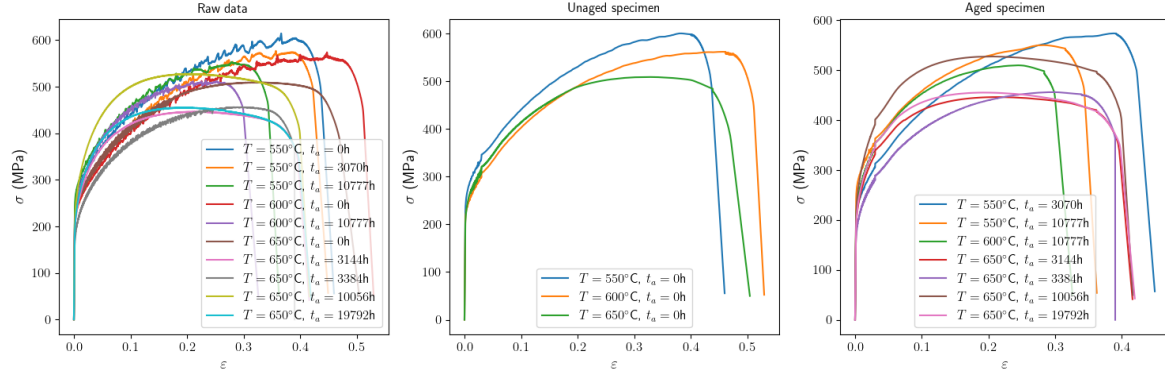


Figure 4.1: Stress-strain curves of the high-temperature uniaxial tension tests. (left) Raw data. (middle) Smoothed tension test data of unaged specimen. (right) Smoothed tension test data of aged specimen.

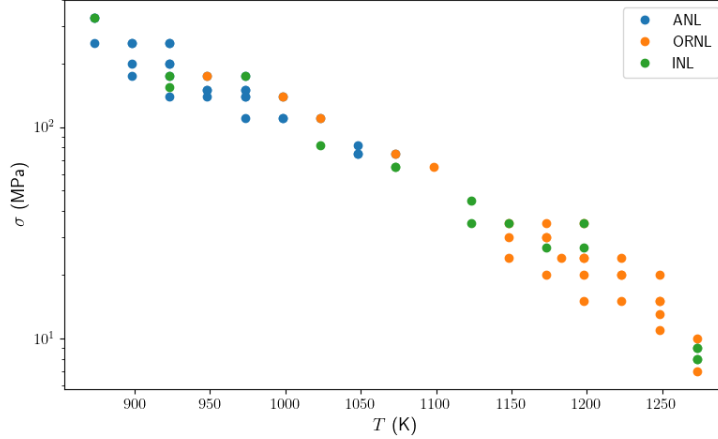


Figure 4.2: The test conditions of the creep tests.

- The large problem size makes the optimization problem ill-conditioned, hence sensitive to the scaling (e.g., normalization of parameters) and the initial guess. The final results may be less accurate.

Therefore, we adopt a progressive calibration approach based on the observations that several types of material responses can be effectively decoupled, i.e., the material response (hence the parameters) can be categorized into (1) short-term response, (2) long-term thermal aging effects, and (3) long-term softening effects due to grain boundary cavitation. Section 4.1 describes the calibration of parameters that control short-term response, Section 4.2 discusses the calibration of long-term thermal aging effects, and Section 4.3 describes the preliminary calibration procedure of a subset of the grain-boundary cavitation parameters.

Table 4.1: Summary of material properties and model parameters in the constitutive models for alloy 709 (excluding the precipitate-specific parameters which are summarized in separate tables). Physical constants such as R , k and Na are not listed. A consistent unit system of [s, mm, Mg, K, mmol] is used. Values ranging from 500°C to 900°C are presented with a uniform interval of 200°C. In the actual numerical simulations, a finer grid with uniform interval of 50°C is used. Values that are unavailable from literature or ThermoCalc are left empty.

Name	Symbol	@ 500°C	@ 700°C	@ 900°C	Source
Shear modulus	G	73 643	64 728	59 689	[8, 9]
Burgers vector magnitude	b	2.5×10^{-7}	2.5×10^{-7}	2.5×10^{-7}	[3]
Reference flow rate	$\dot{\gamma}_0$				
Plastic flow exponent	n				
Interaction coef.	α_d				
Initial dislocation spacing	$L_{d,0}$				
Self-hardening coef.	J_1				
Latent-hardening coef.	J_2				
Reference static recovery coef.	K_0				
Static recovery activation energy	Q_K				
Interaction coef.	α_p				
Interaction coef.	α_s				
Chromium total concentration	c_0	0.199	0.199	0.199	ThermoCalc
Chromium equilibrium concentration	c^*	0.130	0.180	0.189	ThermoCalc
Molybdenum total concentration	c_0	0.015	0.015	0.015	ThermoCalc
Molybdenum equilibrium concentration	c^*	0.001	0.010	0.013	ThermoCalc
Initial avg. cavity radius	a_0	4×10^{-5}	4×10^{-5}	4×10^{-5}	
Initial avg. cavity half spacing	b_0	5×10^{-2}	5×10^{-2}	5×10^{-2}	
Reference nucleation rate	F_N				
Reference traction	Σ_0				
Nucleation exponent	γ				
Critical number density	N_c				
Cavity diffusivity	D				
Cavity shape angle	ψ	75°	75°	75°	[3]
Damage softening exponent	m	0.5	0.5	0.5	

4.1 Calibration of short-term creep responses

The short-term responses are by definition time-insensitive and identifiable from the initial portion of the tension tests and creep tests. 5 out of the 18 parameters control the short-term creep responses of Alloy 709: the initial dislocation spacing $L_{d,0}$, the self- and latent-hardening coefficients J_1 and J_2 , the reference flow rate $\dot{\gamma}_0$, and the power-law creep exponent n .

The self-hardening coefficient J_1 is assumed to scale proportionally with the shear modulus. The latent hardening coefficient J_2 is assumed to scale proportionally with J_1 , and the ratio between J_1 and J_2 is assumed to be temperature-independent. The initial guesses for $L_{d,0}$, J_1 and J_2 are obtained with preliminary manual calibration. The initial guesses for the

Table 4.2: Summary of material properties and model parameters for the carbide phase.

Name	Symbol	@ 500°C	@ 700°C	@ 900°C	Source
Ini. precip. radius	r_i	1.54×10^{-4}	1.54×10^{-4}	1.54×10^{-4}	[9] & ThermoCalc
Ini. precip. number density	N_i	1.07×10^3	1.07×10^3	1.07×10^3	[9]
Reference diffusivity	D_0	1.5×10^2	1.5×10^2	1.5×10^2	[10]
Diffusion activation energy	Q_D	2.4×10^5	2.4×10^5	2.4×10^5	[10]
Interface energy	χ	3×10^{-7}	3×10^{-7}	3×10^{-7}	[10]
Reference nucleation rate	N_0				
Molecular volume	$\text{Na} \cdot \omega$	6.5	6.5	6.5	ThermoCalc
Lattice parameter	a_m	3.6×10^{-7}	3.6×10^{-7}	3.6×10^{-7}	[3]
Solubility coarsening factor	C_f	1	1	1	[3]
Cr precipitate concentration	c_p	0.715	0.695	0.680	ThermoCalc
Mo precipitate concentration	c_p	0.185	0.186	0.144	ThermoCalc

Table 4.3: Summary of material properties and model parameters for the Laves phase.

Name	Symbol	@ 500°C	@ 700°C	@ 900°C	Source
Ini. precip. radius	r_i	1.54×10^{-4}	1.54×10^{-4}	1.54×10^{-4}	[9] & ThermoCalc
Ini. precip. number density	N_i	1.50×10^3	1.50×10^3	1.50×10^3	[9]
Reference diffusivity	D_0	7.4×10^2	7.4×10^2	7.4×10^2	[10]
Diffusion activation energy	Q_D	2.83×10^5	2.83×10^5	2.83×10^5	[10]
Interface energy	χ	2.5×10^{-7}	2.5×10^{-7}	2.5×10^{-7}	[10]
Reference nucleation rate	N_0				
Molecular volume	$\text{Na} \cdot \omega$	8.15	8.15	8.15	ThermoCalc
Lattice parameter	a_m	3.6×10^{-7}	3.6×10^{-7}	3.6×10^{-7}	[3]
Solubility coarsening factor	C_f	1	1	1	[3]
Cr precipitate concentration	c_p	0.202	N/A	N/A	ThermoCalc
Mo precipitate concentration	c_p	0.461	N/A	N/A	ThermoCalc

Table 4.4: Summary of material properties and model parameters for the nitride phase.

Name	Symbol	@ 500°C	@ 700°C	@ 900°C	Source
Ini. precip. radius	r_i	1.54×10^{-4}	1.54×10^{-4}	1.54×10^{-4}	[9] & ThermoCalc
Ini. precip. number density	N_i	1×10^3	1×10^3	1×10^3	[9]
Reference diffusivity	D_0	2.29×10^2	2.29×10^2	2.29×10^2	[10]
Diffusion activation energy	Q_D	2.44×10^5	2.44×10^5	2.44×10^5	[10]
Interface energy	χ	2.5×10^{-7}	2.5×10^{-7}	2.5×10^{-7}	[10]
Reference nucleation rate	N_0				
Molecular volume	$\text{Na} \cdot \omega$	9.7	9.7	9.7	ThermoCalc
Lattice parameter	a_m	3.6×10^{-7}	3.6×10^{-7}	3.6×10^{-7}	[3]
Solubility coarsening factor	C_f	1	1	1	[3]
Cr precipitate concentration	c_p	0.825	0.803	0.807	ThermoCalc
Mo precipitate concentration	c_p	0.057	0.073	0.033	ThermoCalc

reference flow rate γ_0 and the power-law exponent n are obtained using the Kocks-Mecking

relationship, i.e.

$$\ln\left(\frac{\sigma}{G}\right) = \frac{AkT}{Gb^3} \ln\left(\frac{\dot{\varepsilon}_0}{\dot{\varepsilon}}\right) + B. \quad (4.1)$$

which can be rewritten as

$$\dot{\varepsilon} = \dot{\varepsilon}_0 \exp\left(\frac{BGb^3}{AkT}\right) \left(\frac{\sigma}{G}\right)^{-\frac{Gb^3}{AkT}}. \quad (4.2)$$

(4.2) suggests that, for primary creep following a power-law,

$$n = -\frac{Gb^3}{AkT}, \quad \dot{\gamma}_0 \approx \dot{\varepsilon}_0 \exp(-Bn), \quad (4.3)$$

where A and B are the slope and intercept of the Kocks-Mecking fitting, respectively. To fine tune the parameters for Alloy 709, the reference flow rate $\dot{\gamma}_0$ is further assumed to be temperature-dependent following an Arrhenius type relation, i.e.,

$$\dot{\gamma}_i = \dot{\gamma}_0 \exp\left(-\frac{Q_g}{RT}\right) \left|\frac{\tau_i}{\tau_{c,i}}\right|^n \text{sgn}(\tau_i), \quad (4.4)$$

where Q_g is the activation energy for the reference flow rate. Combining (4.3) and (4.4), the calibration problem for $\dot{\gamma}_0$ and n can be reparameterized as the calibration problem for $\dot{\gamma}_0$, Q_g , and A . Together with the dislocation forest hardening parameters $L_{d,0}$, J_1 , and J_2 , the 6 parameters that control the short-term responses are calibrated against the tension test results of the as-received specimen and the creep tests. The objective function of the optimization problem is defined as

$$f = w_{\sigma_y} \text{MRE}(\sigma_y, \sigma_y^*) + w_H \text{MRE}(H, H^*) + w_{\dot{\varepsilon}_{\text{pr}}} \text{MRE}(\bar{\dot{\varepsilon}}_{\text{pr}}, \bar{\dot{\varepsilon}}_{\text{pr}}^*), \quad (4.5)$$

where σ_y is the yield stress, H is the linear approximation of the initial hardening, and $\bar{\dot{\varepsilon}}_{\text{pr}}$ is the primary creep strain rate normalized according to the Kocks-Mecking relationship. The quantities subscripted with an asterisk denote quantities derived from experimental measurements. MRE is the mean-relative error defined as

$$\text{MRE}(x, x^*) = \sqrt{\frac{\sum_i (x_i - x_i^*)^2}{\sum_i (x_i^*)^2}}. \quad (4.6)$$

The contributions to the total objective function from each individual MRE are scaled by constant factors

$$w_{\sigma_y} = 0.1, \quad w_H = 0.1, \quad w_{\dot{\varepsilon}_{\text{pr}}} = 0.8, \quad (4.7)$$

stating that the fitting accuracy of the primary creep strain rate is more important than those of the yield stress and hardening slope. The optimization problem is formally stated

as

$$(L_{d,0}, J_1, J_2, A, \dot{\gamma}_0, Q_g) = \arg \min f, \quad (4.8a)$$

$$\text{subject to } L_{d,0} \geq 0, \quad (4.8b)$$

$$J_1 \geq 0, \quad (4.8c)$$

$$J_2 \geq 0, \quad (4.8d)$$

$$A \leq 0, \quad (4.8e)$$

$$\dot{\gamma}_0 \geq 0, \quad (4.8f)$$

$$Q_g \geq 0. \quad (4.8g)$$

The optimization problem (4.8) is solved using the Nelder-Mead algorithm. It is assumed that the grain boundary cavitation effects are negligible in the short-term responses, and so the objective function (4.8) can be evaluated using the standard Taylor approximation of the polycrystal model. The homogenized Cauchy stress is approximated as

$$\boldsymbol{\sigma} = \frac{1}{N_p} \sum_i \boldsymbol{\sigma}_i, \quad (4.9)$$

where N_p is the number of crystals, and $\boldsymbol{\sigma}_i$ is the Cauchy stress of each crystal. In the current study, 40 crystals are used to evaluate the objective function.

The fitted parameters are summarized in Table 4.5. Again, representative values are sampled at 500°C, 700°C, and 900°C. A finer grid with uniform spacing of 50°C is used in the actual simulations.

Table 4.5: Summary of calibrated parameters that control the short-term responses.

Name	Symbol	@ 500°C	@ 700°C	@ 900°C
Ini. dislocation spacing	$L_{d,0}$	2.72×10^{-4}	2.72×10^{-4}	2.72×10^{-4}
Self hardening coef.	J_1	3.59×10^8	3.15×10^8	2.91×10^8
Latent hardening coef.	J_2	44 560.1	39 166.0	36 117.1
Reference flow rate	$\dot{\gamma}_0$	1.41×10^{-12}	2.72×10^{-8}	1.82×10^{-5}
Plastic flow exponent	n	11.0	7.68	5.88

The primary creep strain rates obtained using the fitted model are compared with those obtained using the experimental data in Figure 4.3.

4.2 Calibration of thermal aging effects

Thermal aging is affected by the dislocation recovery mechanism, the precipitation hardening, and the solid solution strengthening. Only temperature-dependent static recovery is considered in the Alloy 709 model, which is controlled by the reference static recovery coefficient K_0 and the static recovery activation energy Q_K . Most of the parameters in the Hu-Cocks model are selected based on ThermoCalc calculations or from various literature sources, as listed in Tables 4.2, 4.3, and 4.4. The interaction coefficients α_d , α_p , and α_s control the relative contribution to the overall hardening from each hardening mechanism,

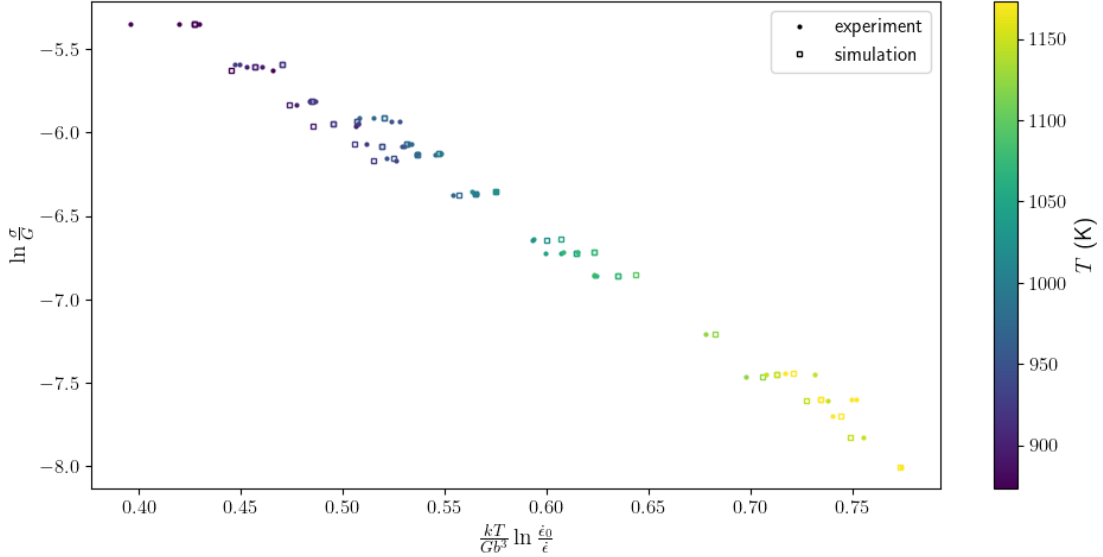


Figure 4.3: The calibrated Kocks-Mecking relationship. Simulated data are plotted as dots, and the experimental data are plotted as squares. The data points are colored according to the temperature.

and there are infinitely many minimizers for the interaction coefficients. For the purpose of calibration, we fix $\alpha_d = 1$ and calibrate the other two interaction coefficients α_p and α_s . The precipitate reference nucleation rates N_0 are unavailable from ThermoCalc or the literature, and they are calibrated along with the other parameters. Both the interaction coefficients and the precipitate reference nucleation rates are assumed to be temperature-independent in the current work.

In summary, a total of 7 parameters are calibrated against the tension tests: K_0 , Q_K , α_p , α_s , and N_0 (one for each of the three precipitates). These parameters are calibrated against the 3 “unaged” tension tests and the 7 “aged” tension tests at various temperatures. For static dislocation recovery, the tension tests are simulated up 60% of the ultimate tensile strength (approximated based on the experimental measurements). The error is computed as the MRE of the hardening slope, i.e. $\partial\sigma/\partial\varepsilon$. For thermal aging, the same aging conditions as the experiments are simulated, after which uniaxial tension tests are simulated. The error is computed as the MRE of the yield stress post-aging. The objective function is defined as

$$f = w_H \text{MRE}(H, H^*) + w_{\sigma_y} \text{MRE}(\sigma_y, \sigma_y^*), \quad (4.10)$$

with prefactors

$$w_H = w_{\sigma_y} = 0.5, \quad (4.11)$$

stating that the static recovery mechanism and the Hu-Cocks aging mechanisms are equally

important during the fitting process. The optimization problem is formally stated as

$$(K_0, Q_K, \alpha_p, \alpha_s, N_{0,i}) = \arg \min f, \quad (4.12a)$$

$$\text{subject to } K_0 \geq 0, \quad (4.12b)$$

$$Q_K \geq 0, \quad (4.12c)$$

$$\alpha_p \geq 0, \quad (4.12d)$$

$$\alpha_s \geq 0, \quad (4.12e)$$

$$N_{0,i} \geq 0. \quad (4.12f)$$

The optimization problem (4.12) is solved using the Nelder-Mead algorithm. Taylor approximation to the homogenized Cauchy stress (see e.g. Section 4.1) is again used to evaluate the objective function. The fitted parameters are summarized in Table 4.6. The fitting suggests that the initial strengthening of the Alloy 709 is mainly attributed to the nucleation of the laves phase precipitates.

Table 4.6: Summary of calibrated parameters that control the thermal aging effects.

Name	Symbol	@ 500°C	@ 700°C	@ 900°C
Static recovery coef.	K	2.39×10^{-20}	1.33×10^{-19}	4.10×10^{-19}
Int. coef. for precip. hardening	α_p	2.17×10^{-3}	2.17×10^{-3}	2.17×10^{-3}
Int. coef. for solid solution hardening	α_s	7.32×10^{-8}	7.32×10^{-8}	7.32×10^{-8}
Carbide ref. nucleation rate	N_0	5.53×10^{-4}	5.53×10^{-4}	5.53×10^{-4}
Laves ref. nucleation rate	N_0	31.3	31.3	31.3
Nitride ref. nucleation rate	N_0	0	0	0

4.3 Preliminary calibration of the grain boundary cavitation model

In Section 4.1, 5 parameters related to the short-term responses have been calibrated. In Section 4.2, 8 parameters related to the thermal aging effects have been calibrated. At this point, 13 out of the 18 unknown parameters in Tables 4.1, 4.2, 4.3, and 4.4 have been calibrated, and only 5 parameters that are related to the grain boundary cavitation model are left. Based on previous sensitivity studies [11, 12], the cavity diffusivity D are the reference nucleation rate F_N are the most influential parameters on the prediction of tertiary creep and rupture, and will be comprehensively calibrated using the combination of CPFE simulations and Bayesian inference (Chapter 5). On the other hand, the reference traction Σ_0 , the nucleation exponent γ , and the critical number density N_c are bounded using the expedition simulations, a special type CPFE simulation excluding the effects of grain boundary cavitation.

First, a “test” plan is designed for the expedition CPFE simulation campaign. The campaign is designed to cover the range over which ThermoCalc data is available with a uniform temperature interval of 50°C. At each temperature, 5 different stresses uniformly distributed on the log-scale are planned to cover the experimental conditions. The test plan for the expedition CPFE simulation campaign is illustrated in Figure 4.4.

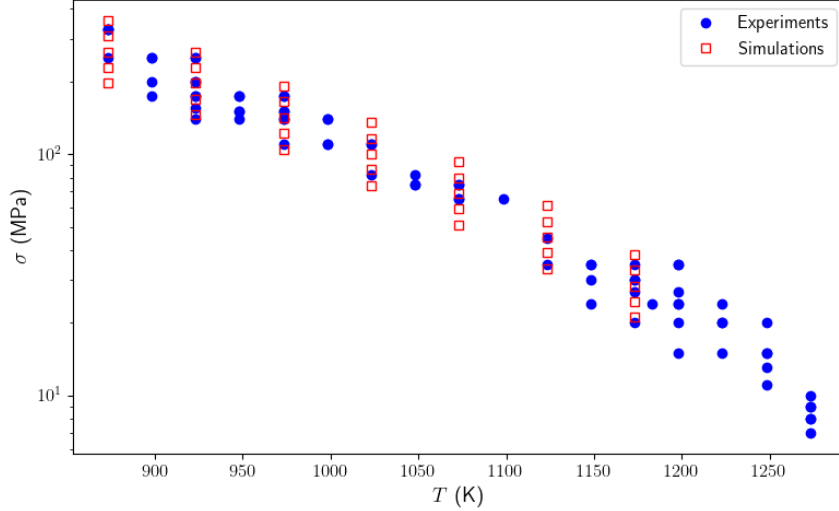


Figure 4.4: Test plan for the expedition CPFE simulation campaign.

According to the test plan, a total of 35 CPFE simulations (with a specific realization of RVE) are carried out using the setup described in Chapter 2. The simulated strain and strain rate are plotted in Figure 4.5. In each CPFE simulation, the complete time series of the cavitation “driving forces” are recorded. The driving forces include: the normal traction at the grain boundaries, the equivalent creep strain, the von Mises stress, and the hydrostatic stress. Based on the assumption that, before tertiary creep, the interface traction at the grain boundaries is only weakly coupled with the softening induced by grain boundary cavitation, the grain boundary cavitation model (Section 3.3) can be treated as ordinary differential equations (ODEs) to predict the onset of tertiary creep. The objective function for the optimization problem is defined as

$$f = \text{MRE}(\ln(t_t), \ln(t_t^*)), \quad (4.13)$$

where t_t is the time-to-tertiary. The optimization problem is formally stated as

$$(\Sigma_0, \gamma, N_c) = \arg \min f, \quad (4.14a)$$

$$\text{subject to } \Sigma_0 \geq 0, \quad (4.14b)$$

$$\gamma \geq 0, \quad (4.14c)$$

$$N_c \geq 0. \quad (4.14d)$$

The optimization problem (4.14) is solved using the Nelder-Mead algorithm. The cavity diffusivity and the reference nucleation rate are assumed to be temperature dependent following the Arrhenius-type relations, i.e.

$$D = D_0 \exp\left(-\frac{Q_D}{RT}\right), \quad F_N = F_{N,0} \exp\left(-\frac{Q_{F_N}}{RT}\right). \quad (4.15)$$

The other parameters are assumed to be temperature independent. The fitted parameters are summarized in Table 4.7. Predictions made by the fitted grain boundary cavitation parameters (using the driving forces approximated using the expedition CPFE simulations) are plotted in Figure 4.6.

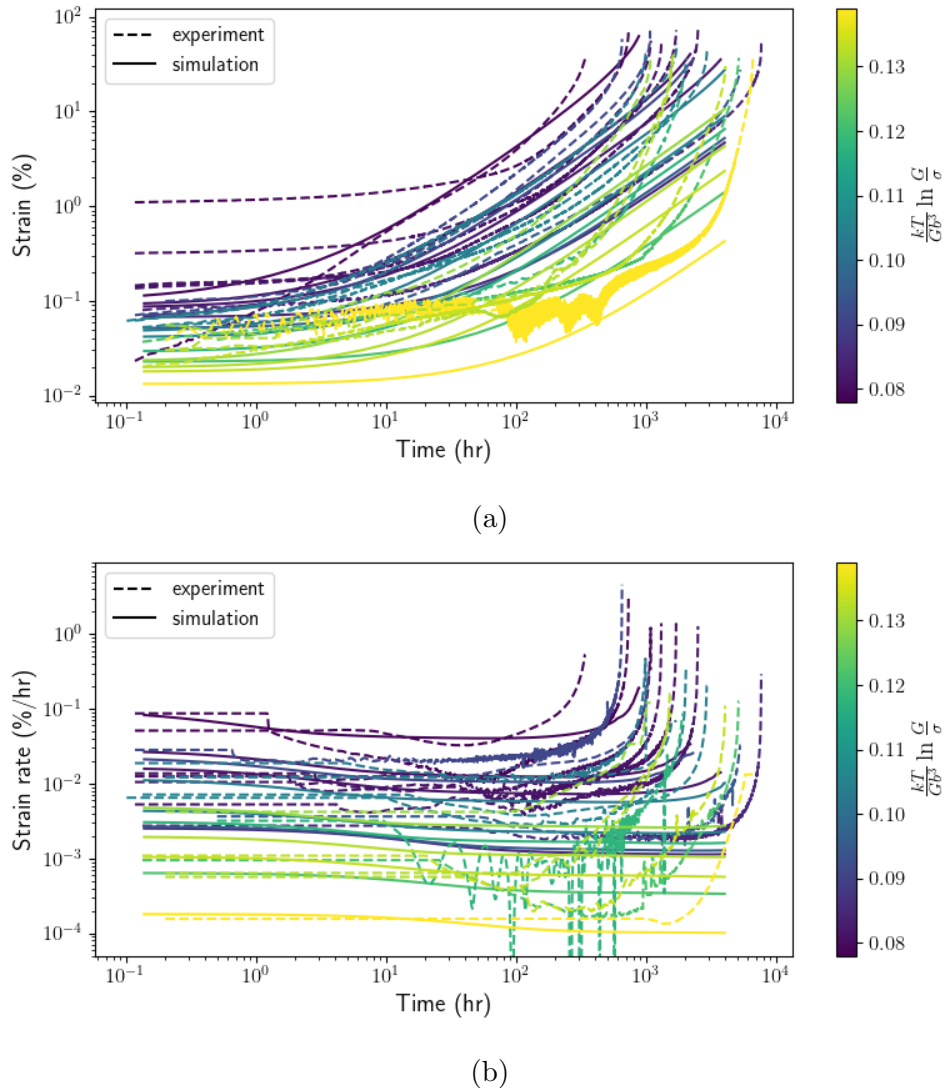


Figure 4.5: (a) Total strain and (b) strain rate as functions of time from the expedition CPFE simulations. The simulated curves are plotted as solid lines, and the experimental curves are plotted as dashed lines. The curves are colored using the pseudo Kocks-Mecking normalization.

Table 4.7: Summary of the initial calibration of grain boundary cavitation parameters.

Name	Symbol	@ 700°C	@ 800°C	@ 900°C
Cavity diffusivity	D	3.75×10^{-12}	1.08×10^{-11}	2.59×10^{-11}
Reference nucleation rate	F_N	3.71×10^5	9.47×10^5	2.06×10^6
Reference normal traction	Σ_0	254.0	254.0	254.0
Cavity nucleation exponent	γ	0.371	0.371	0.371
Critical number density	N_c	2.99×10^{-4}	2.99×10^{-4}	2.99×10^{-4}

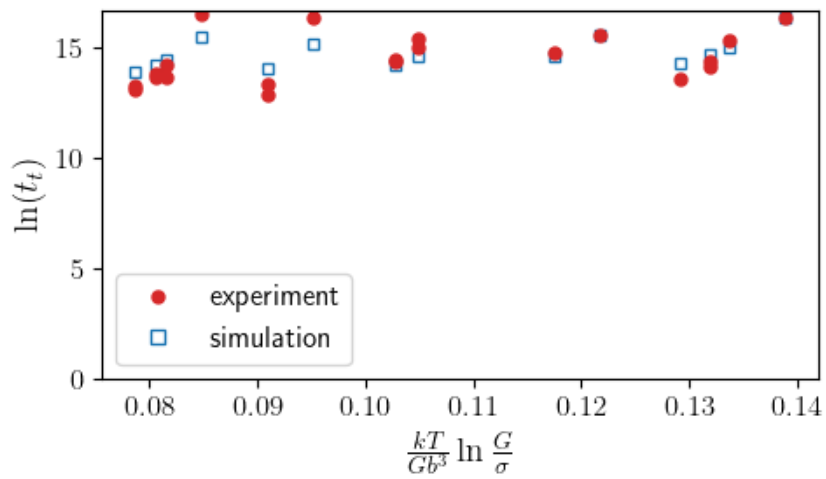


Figure 4.6: The time-to-tertiary predictions using the fitted grain boundary cavitation parameters from Table 4.7. Simulated times-to-tertiary are plotted as blue squares, and the experimental times-to-tertiary are plotted as red dots.

5 Inference for the remaining parameters

Section 4.3 described an efficient way of obtaining initial guesses for the grain boundary cavitation parameters. The initial model has a reasonable accuracy based on the expedition CPFE simulation results (Figure 4.6). Recall the fundamental assumption made in the expedition CPFE simulation campaign: the traction-separation relation and the softening due to grain boundary cavitation can be effectively decoupled prior to the onset of tertiary creep. This assumption enabled the efficient initial calibration, however, its validity is questionable especially in the context of physics-based extrapolation of creep rupture. Since the sensitivity studies suggest that the cavity diffusivity D and the cavity reference nucleation rate F_N are the most influential parameters in the prediction of time-to-tertiary, they are “re-calibrated” using stochastic variational inference (SVI) in Section 5.3. Since statistical inference requires (1) a large number of forward evaluations and (2) the parameter gradients of the objective function, CPFE simulation is computationally intractable¹ to be directly used as the forward evaluation method. To reduce the computational cost, a surrogate model (Section 5.2) is trained based on full-fledged CPFE simulations (Sections 5.1).

5.1 Simulation campaign setup

First, a similar test plan as the expedition simulation campaign (Section 4.3) is designed to generate a reasonable coverage of experimental testing conditions. The test plan is illustrated in Figure 5.1. A log-uniform grid of 5 applied stress loads is used at each temperature. 600°C and 650°C are excluded from the test plan because tertiary creep is primarily driven by the combination of hardening exhaustion and necking at those temperatures (see e.g. Figure 4.5), and so the onset of tertiary is relatively insensitive to the grain boundary cavitation parameters.

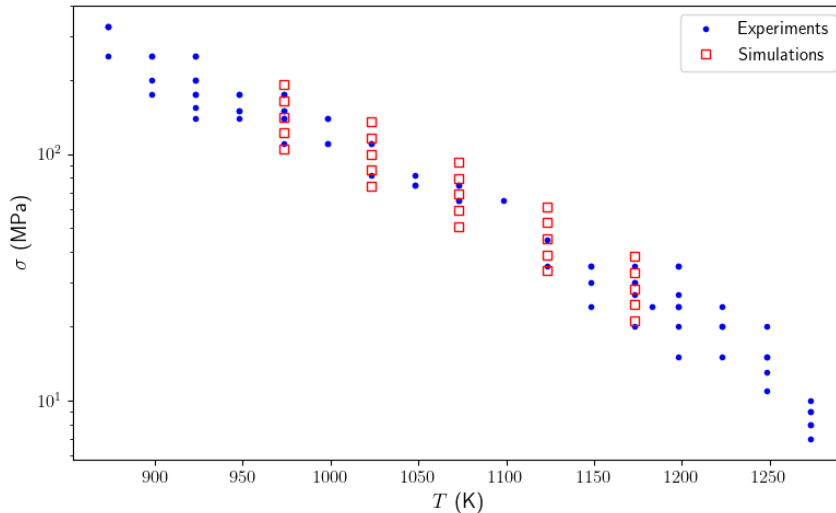


Figure 5.1: Test plan for the full-fledged CPFE simulation campaign.

In order to generate predictions that cover the range of experimental times-to-tertiary, a

¹Typically, a single evaluation of the objective function using the CPFE model can take weeks.

total of 81 combinations of grain boundary cavitation parameters (Figure 5.2) are generated by perturbing the preliminary calibration from Section 4.3. The reference cavity diffusivity and the reference nucleation rate are perturbed by 50% about their initial guesses, and their corresponding activation energies are perturbed by 20% about the initial guesses.

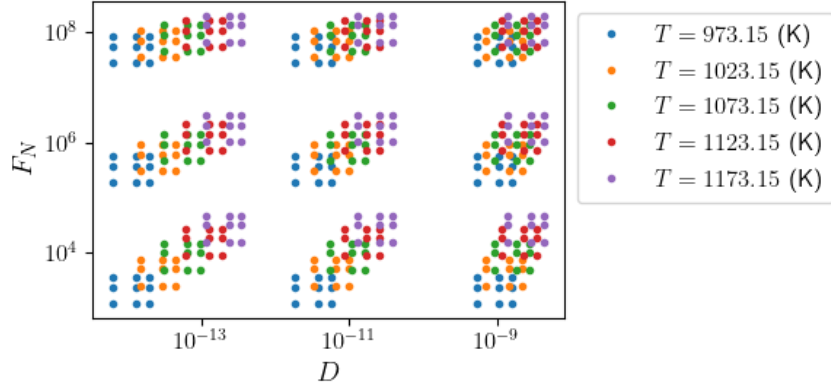


Figure 5.2: Grain boundary cavitation parameters used in the full-fledged CPFE simulation campaign.

Combining the microstructure realization (Section 2.1), the plan for testing conditions (Figure 5.1), and the grain boundary cavitation parameter combinations (Figure 5.2), a campaign consisting of $10 \times 25 \times 81 = 20250$ CPFE simulations is fully specified. With the available computing resource allocated for the current project, 8359 CPFE simulations are complete, covering microstructure realizations 1 through 4, plus part of microstructure realization 5. A slight deviation from the fully converged statistics as more simulations become available is expected according to the convergence study (Figure 2.3).

5.2 Surrogate modeling

To reduce the computational resources required to calibrate the grain boundary cavitation model, a surrogate model is developed. The surrogate model approximates the time-to-tertiary given the test conditions and a set of material parameters, i.e.

$$t_t = f(T, \sigma; D, F_N), \quad (5.1)$$

where t_t is the time-to-tertiary, D is the cavity diffusivity, F_N is the reference cavity nucleation rate, and the test conditions are temperature T and the applied load σ . With the surrogate model, a single evaluation of the objective function can be completed in seconds instead of weeks. This allows the surrogate model to replace the CPFE model during the inference process, given that the surrogate model has a reasonable accuracy.

Times-to-tertiary with the same testing condition on different RVE realizations are averaged to provide the mean response. CPFE simulations that terminated before tertiary creep are excluded from the dataset. 75% of the simulations are used as the training set, and the rest 25% of the simulations are used as the validation set. All 5 features (4 input features and 1 output feature) are normalized based on the training set.

A deep neural network (DNN) is used as a surrogate model. The inputs of the DNN are the test conditions (temperature and applied stress) and the material parameters (cavity diffusivity D and cavity nucleation rate F_N), whereas the output of the DNN is the average time-to-tertiary. The network consists of 3 hidden layers of size 32, 16, and 8, respectively, each followed by a standard sigmoid activation function. The standard mean-squared error $\text{MSE}(t_t)$ of the normalized time-to-tertiary is used as the loss function. The surrogate model is trained using the standard Adam optimizer with initial learning rate of 1×10^{-3} and L_1 regularization coefficient of 1×10^{-6} . The learning rate is adaptively reduced by a factor of 10 with a patience of 200 epochs. The training process is early stopped if the learning rate drops below 1×10^{-6} to prevent overfitting.

A comparison of the surrogate model's predictions and the CPFE predictions for the time-to-tertiary is shown in Figure 5.3. The proximity of the data points to the 1:1 line suggests that the surrogate model is able to predict the time-to-tertiary with high accuracy.

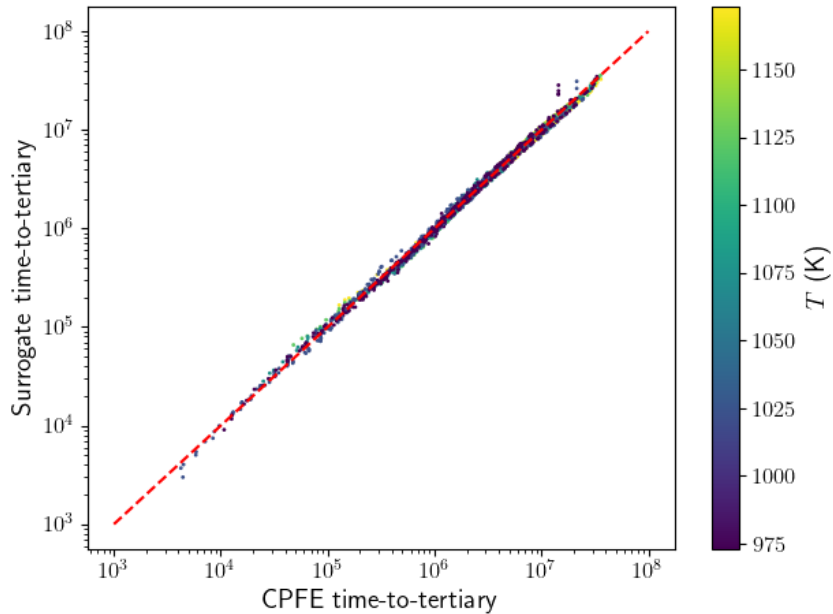


Figure 5.3: Comparison between the surrogate model's time-to-tertiary prediction and the CPFE model's time-to-tertiary prediction.

5.3 Statistical inference

The entire calibration procedure is closed by inferring the last two unknown material properties: the cavity diffusivity D and the reference cavity nucleation rate F_N . We use Stochastic Variational Inference (SVI) to find maximum a posteriori estimates of the parameterized distributions for these parameters. The CPFE model and hence the corresponding surrogate model are now treated as stochastic processes that propagate the uncertainties in D and F_N .

The deterministic forward problem (5.1) is replaced by its stochastic counterpart

$$t_t \sim \mathcal{N}(f(D, F_N), \epsilon^2), \quad (5.2a)$$

$$D \sim \mathcal{N}(\mu_D, \sigma_D^2), \quad (5.2b)$$

$$F_N \sim \mathcal{N}(\mu_{F_N}, \sigma_{F_N}^2), \quad (5.2c)$$

where $\mathcal{N}(\mu, \sigma)$ denotes a normal distribution with mean μ and standard deviation σ . ϵ is the white noise in the observation of the time-to-tertiary that are not modeled through the random processes associated with D and F_N . The parameterized distributions are optimized to maximize the standard ELBO loss, i.e.

$$(\mu_D, \sigma_D, \mu_{F_N}, \sigma_{F_N}) = \arg \max \text{ELBO}(3t_t, t_r), \quad (5.3)$$

where gradient steps are taken by conditioning the samples t_t on experimental evidence t_r . The standard Leyda Rowe relation is used to relate time-to-tertiary t_t predicted by the surrogate model and time-to-rupture (creep life) recorded in the experiments. The optimization problem (5.3) is solved on the normalized dataset: the same normalizers from the surrogate model is used on latent random variables D and F_N ; the normalizer for the time-to-tertiary is used to normalize both the random variable t_t and the experimental observation t_r . 5000 gradient steps are taken using the Adam algorithm with a learning rate of 1×10^{-3} . (5.3) is repeated for each temperature². The inferred parameters as functions of temperature and their 90% confidence bounds are plotted in Figure 5.4. There are two

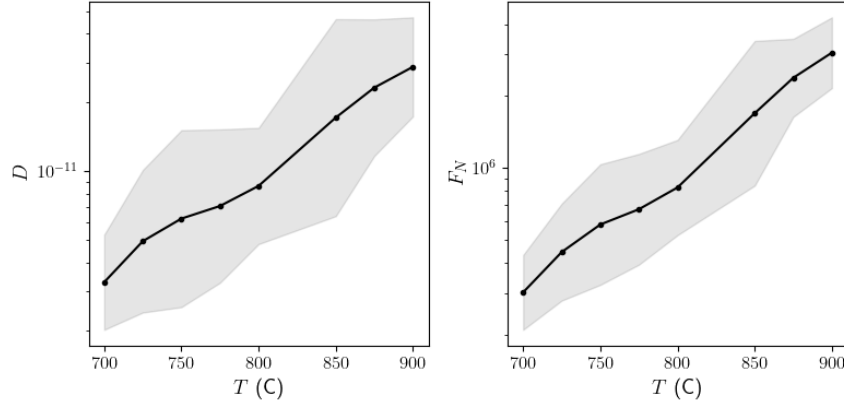


Figure 5.4: The grain boundary cavitation parameters inferred by solving (5.3). (left) Cavity diffusivity as a function of temperature. (right) Reference cavity nucleation rate as a function of temperature. Mean values of posterior estimates are plotted as solid black lines. The 90% confidence intervals are indicated using gray shadow.

plausible forms of functional dependence on temperature of the grain boundary cavitation parameters based on observation of the log-scale plots: a linear dependence and an Arrhenius type dependence. Since both parameters have supports on $(0, \infty)$, it is hereinafter assumed

²Temperature 825°C is excluded as only one observation is available, which results in a rank-deficient system.

that the grain boundary cavitation model shall include a thermal activation mechanism described as

$$D = 8.651 \times 10^{-7} \cdot \exp\left(\frac{1.011 \times 10^5}{RT}\right), \quad (5.4a)$$

$$F_N = 1.804 \times 10^{11} \cdot \exp\left(\frac{1.079 \times 10^5}{RT}\right). \quad (5.4b)$$

The observation (5.4) is useful especially when using the physics-based model to extrapolate, i.e., to predict the material's creep life outside the range of temperatures where experimental data is available. The posterior estimate of time-to-tertiary is shown in Figure 5.5.

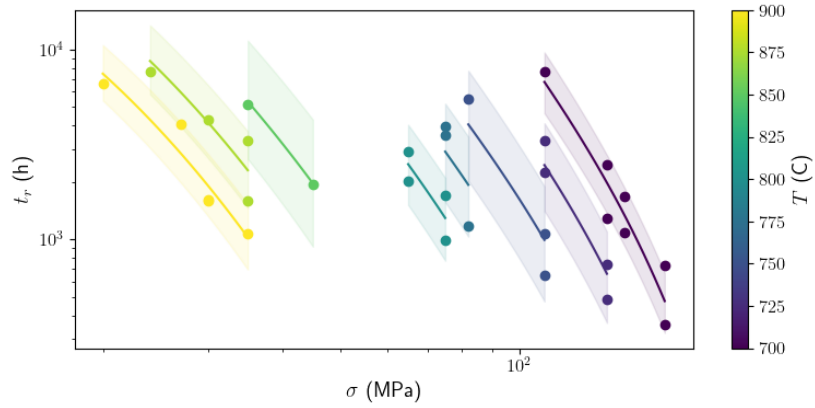


Figure 5.5: The posterior estimates of time-to-rupture t_r predictions at different temperatures. Experimental observations are marked as dots. Mean predictions are plotted as solid lines. The 90% confidence intervals are indicated using light shadows of the same color. All points are color-coded based on the temperature.

6 Long-term predictions

6.1 The calibrated constitutive model for Alloy 709

For completeness and convenience, the complete set of material properties and model parameters for Alloy 709 are summarized in the following tables. It is worth emphasizing that the calibrated and inferred material properties and model parameters are not necessarily the real (e.g. as measured) values. They are, however, the best estimates given the available experimental data, and, as shown in the previous chapters on the calibration procedure (Chapters 4 and 5), the resulting constitutive model for Alloy 709 fits available experimental data reasonably well.

Table 6.1: Summary of material properties and model parameters in the constitutive models for alloy 709 (excluding the precipitate-specific parameters which are summarized in separate tables). Physical constants such as R , k and Na are not listed. A consistent unit system of [s, mm, Mg, K, mmol] is used. Values ranging from 500°C to 900°C are presented with a uniform interval of 200°C. In the actual numerical simulations, a finer grid with uniform interval of 50°C is used.

Name	Symbol	@ 500°C	@ 700°C	@ 900°C
Shear modulus	G	73 643	64 728	59 689
Burgers vector magnitude	b	2.5×10^{-7}	2.5×10^{-7}	2.5×10^{-7}
Chromium total concentration	c_0	0.199	0.199	0.199
Chromium equilibrium concentration	c^*	0.130	0.180	0.189
Molybdenum total concentration	c_0	0.015	0.015	0.015
Molybdenum equilibrium concentration	c^*	0.001	0.010	0.013
Initial avg. cavity radius	a_0	4×10^{-5}	4×10^{-5}	4×10^{-5}
Initial avg. cavity half spacing	b_0	5×10^{-2}	5×10^{-2}	5×10^{-2}
Cavity shape angle	ψ	75°	75°	75°
Damage softening exponent	m	0.5	0.5	0.5

Table 6.2: Summary of calibrated parameters that control the short-term responses.

Name	Symbol	@ 500°C	@ 700°C	@ 900°C
Ini. dislocation spacing	$L_{d,0}$	2.72×10^{-4}	2.72×10^{-4}	2.72×10^{-4}
Self hardening coef.	J_1	3.59×10^8	3.15×10^8	2.91×10^8
Latent hardening coef.	J_2	44 560.1	39 166.0	36 117.1
Reference flow rate	$\dot{\gamma}_0$	1.41×10^{-12}	2.72×10^{-8}	1.82×10^{-5}
Plastic flow exponent	n	11.0	7.68	5.88

6.2 Predictions of long-term creep rupture

In this section, the calibrated CPFE model for Alloy 709 is used to predict long-term creep (i.e., with creep rupture times ranging approximately from 1×10^4 h to 1×10^6 h) with different rupture stresses at various temperatures (Figure 6.2(a)). A number of grain boundary

Table 6.3: Summary of calibrated parameters that control the thermal aging effects.

Name	Symbol	@ 500°C	@ 700°C	@ 900°C
Static recovery coef.	K	2.39×10^{-20}	1.33×10^{-19}	4.10×10^{-19}
Int. coef. for precip. hardening	α_p	2.17×10^{-3}	2.17×10^{-3}	2.17×10^{-3}
Int. coef. for solid solution hardening	α_s	7.32×10^{-8}	7.32×10^{-8}	7.32×10^{-8}
Carbide ref. nucleation rate	N_0	5.53×10^{-4}	5.53×10^{-4}	5.53×10^{-4}
Laves ref. nucleation rate	N_0	31.3	31.3	31.3
Nitride ref. nucleation rate	N_0	0	0	0

Table 6.4: Summary of the calibrated grain boundary cavitation parameters.

Name	Symbol	@ 700°C	@ 800°C	@ 900°C
Cavity diffusivity	D	3.272×10^{-12}	8.634×10^{-12}	2.868×10^{-11}
Reference nucleation rate	F_N	3.017×10^5	8.286×10^5	3.038×10^6
Reference normal traction	Σ_0	254.0	254.0	254.0
Cavity nucleation exponent	γ	0.371	0.371	0.371
Critical number density	N_c	2.99×10^{-4}	2.99×10^{-4}	2.99×10^{-4}

cavitation parameters are sampled from the inferred posteriors for each rupture stress and temperature. These CPFE simulations for long-term creep complement the database used in Section 5.2 for short-term creep surrogate modeling. The combined database is used to train a new surrogate model that maps from test conditions and grain boundary cavitation parameters to tertiary times for both short- and long-term creep. The new surrogate model is used to generate the 90% confidence interval in the predictions.

The predictions are compared with the classical Larson-Miller approach with a linear and a quadratic polynomial fit. The Larson-Miller approach is based on the time-temperature parameter in the following form

$$\text{LMP} = T(\log_{10}(t_r) + C), \quad (6.1)$$

where C is a constant to be fitted. The Larson-Miller parameter (LMP) is correlated with rupture stress. We consider the polynomial form:

$$\text{LMP}_p = \sum_{i=0}^p c_i (\log_{10}(\sigma))^i, \quad (6.2)$$

where LMP_p indicates the Larson-Miller fit of order p , and c_i are the polynomial coefficients. The unknowns c_i and C are fitted against experimental data using the least-squares fitting. The fitted correlations LMP_1 and LMP_2 can be written as

$$\text{LMP}_1 = T(\log_{10}(t_r) + 13.23) = -4922 \log_{10}(\sigma) + 26\,648, \quad (6.3)$$

$$\text{LMP}_2 = T(\log_{10}(t_r) + 13.96) = -1151 [\log_{10}(\sigma)]^2 - 941 \log_{10}(\sigma) + 24\,086. \quad (6.4)$$

The coefficients of determination are 0.854 and 0.895 for LMP_1 and LMP_2 , respectively. The fitted Larson-Miller correlations are plotted in Figure 6.1.

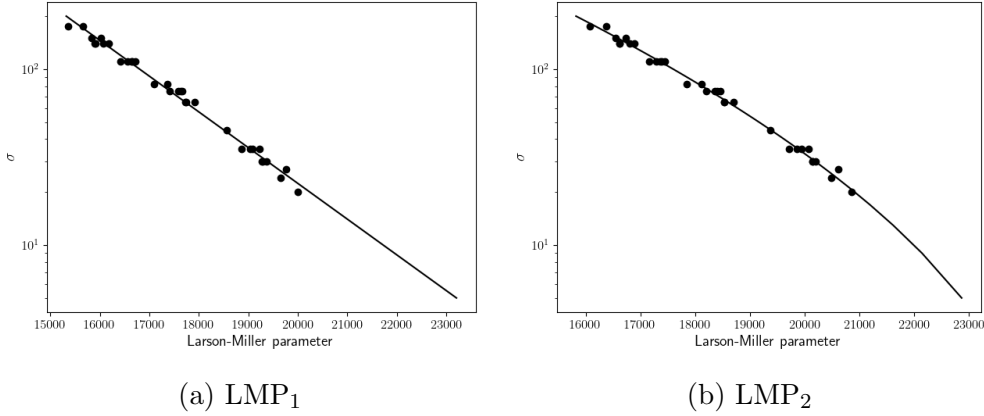


Figure 6.1: The fitted Larson-Miller time-temperature parameters as functions of rupture stress.

The fitted correlation can be used to predict one of the three correlated quantities given the other two. In particular, we use the rupture stress σ and the temperature T to predict time-to-rupture t_r . The predictions are shown in Figure 6.2. Rupture strength predictions at 700K, 800K, and 900K using the three different methods are tabulated in Tables 6.5, 6.6 & 6.7.

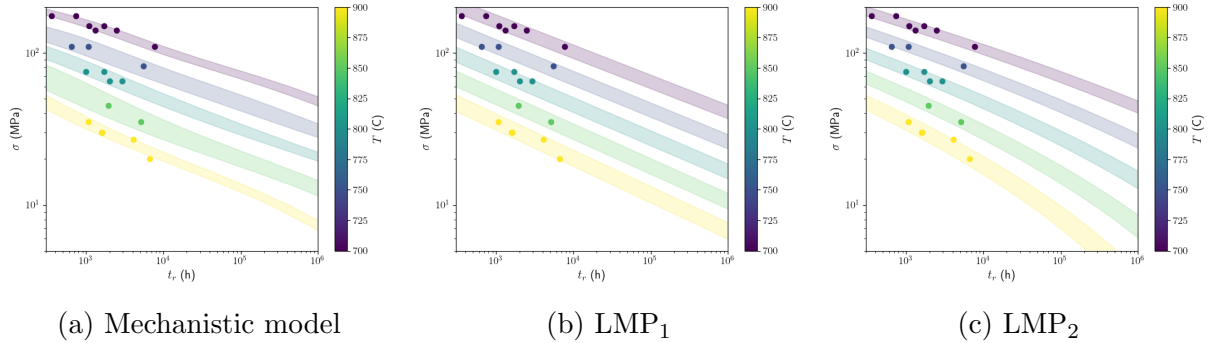


Figure 6.2: Time-to-rupture predictions by (a) the physics-based mechanistic model, (b) the linear Larson-Miller correlation, and (c) the quadratic Larson-Miller correlation. Points are color-coded using the temperature. 90% confidence intervals are shaded.

Table 6.5: Rupture strength (MPa) predictions at 700K

Method	@ 100kh	@ 300kh	@ 500kh
LMP ₁	71.46	57.59	52.07
LMP ₂	75.39	61.42	55.59
Mechanistic	75.95	63.77	58.36

Table 6.6: Rupture strength (MPa) predictions at 800K

Method	@ 100kh	@ 300kh	@ 500kh
LMP ₁	30.83	24.26	21.70
LMP ₂	30.79	23.29	20.31
Mechanistic	34.11	27.83	25.22

Table 6.7: Rupture strength (MPa) predictions at 900K

Method	@ 100kh	@ 300kh	@ 500kh
LMP ₁	13.26	10.22	9.04
LMP ₂	9.86	6.43	5.15
Mechanistic	14.16	11.25	9.82

6.3 Summary and future work

This report describes a physics-based model for predicting long-term creep and thermal aging in Alloy 709. The calibrated model predictions can feed into the DOE:NE ART program effort to qualify this material for long-term, high-temperature service in future advanced reactors. The physics-based approach provides more accurate long-term predictions, compared to empirical time-temperature parameter models, accelerating the qualification of the material by reducing the need for long duration creep tests.

The previous section makes the key comparison between the physics-based model predictions and the Larson-Miller approach commonly applied by ASME. We see two options in applying the physics-based model to qualifying Alloy 709:

1. Use the 90% lower prediction bound from the model to directly provide the extrapolated data required by ASME.
2. While a quadratic Larson-Miller polynomial best fits the short term Alloy 709 data, the physics-based model predictions suggest that a linear Larson-Miller model will better predict long-term creep rupture. These results could therefore suggest formulating the ASME design data using a linear Larson-Miller extrapolation, even though a quadratic fit appears more accurate for the short-term data.

Future work should focus on integrating the model into the ART qualification effort. However, there are also modeling improvements that could be made to the overall framework with the goal of reducing the need to calibrate directly against test data. This could improve the accuracy of the model, but more importantly should reduce the number of full simulations and time required to calibrate the model against test data. Two promising options towards accomplishing this goal could be:

1. Remove all calibration from the precipitation strengthening module by replacing the calibrated Hu-Cocks model with direct kinetic calculations of precipitate nucleation and growth, informed by a physical database. Right now the model's predictions of precipitation are pinned to equilibrium calculations of stable phase fractions. Techniques exist to instead simulate the short-term kinetics of precipitation. However,

coupling these approaches directly into the model could be challenging, as we need a differentiable, continuous model to ensure convergence of the CPFE simulations.

2. Replace the simplified Sham-Needleman representation of diffusion-assisted cavitation with direct simulations of vacancy nucleation and transport. This would eliminate the need to calibrate the Sham-Needleman parameters against test data.

Acknowledgements

This work was sponsored by the U.S. Department of Energy, under Contract No. DE-AC02-06CH11357 with Argonne National Laboratory, managed and operated by UChicago Argonne LLC. Programmatic direction was provided by the Nuclear Energy Advanced Modeling & Simulation Program of the Department of Nuclear Energy. The authors gratefully acknowledge the support and direction of Ben Spencer, at Idaho National Laboratory, National Technical Director Chris Stanek, at Los Alamos National Laboratory, and Federal Manager Dave Henderson as well as the ART materials program, led by Sam Sham of Idaho National Laboratory, for providing material test data.

Bibliography

- [1] J. Hu, G. Green, S. Hogg, R. Higginson, and A. Cocks, “Effect of microstructure evolution on the creep properties of a polycrystalline 316h austenitic stainless steel,” Materials Science and Engineering: A, vol. 772, p. 138787, 2020.
- [2] J. Hu, A theoretical study of creep deformation mechanisms of Type 316H stainless steel at elevated temperatures. PhD thesis, Oxford University, UK, 2015.
- [3] A. Venkataraman and M. Messner, “An initial framework for the rapid qualification of long-term creep rupture strength via microstructural modeling,” Tech. Rep. ANL-21/34, Argonne National Laboratory, 2021.
- [4] O. Nassif, T. J. Truster, R. Ma, K. B. Cochran, D. M. Parks, M. C. Messner, and T. Sham, “Combined crystal plasticity and grain boundary modeling of creep in ferritic-martensitic steels: I. theory and implementation,” Modelling and Simulation in Materials Science and Engineering, vol. 27, no. 7, p. 075009, 2019.
- [5] A. Rovinelli, M. Messner, and T.-L. Sham, “Initial microstructural model for creep-fatigue damage in grade 91 steel,” Tech. Rep. ANL-ART-202, Argonne National Laboratory, 2020.
- [6] L. Svolos, J. N. Plohr, G. Manzini, and H. M. Mourad, “On the convexity of phase-field fracture formulations: Analytical study and comparison of various degradation functions,” International Journal of Non-Linear Mechanics, p. 104359, 2023.
- [7] M. C. Messner, “NEML – Nuclear Engineering Material model Library.”
- [8] V. M. Riso, “Mechanical characterization of alloy 709 stainless steel after high temperature aging for application in advanced reactors,” 2018.
- [9] R. Song, M. D. McMurtrey, and C. D. Clement, “Characterization of alloy 709 commercial heats,” tech. rep., Idaho National Lab.(INL), Idaho Falls, ID (United States), 2021.
- [10] Z. Glowacki and W. Kaluba, “On some features of chromium carbide diffusion layer formation,” Metallurgical Transactions A, vol. 13, pp. 753–759, 1982.
- [11] A. Rovinelli, M. Messner, G. Ye, and T.-L. Sham, “Initial study of notch sensitivity of grade 91 using mechanisms motivated crystal plasticity finite element method,” Tech. Rep. ANL-ART-171, Argonne National Laboratory, 2019.
- [12] A. Behnam, T. J. Truster, R. Tipireddy, M. C. Messner, and V. Gupta, “Uncertainty quantification framework for predicting material response with large number of parameters: Application to creep prediction in ferritic-martensitic steels using combined crystal plasticity and grain boundary models,” Integrating Materials and Manufacturing Innovation, vol. 11, no. 4, pp. 516–531, 2022.

- [13] F. R. Larson and J. Miller, “A time-temperature relationship for rupture and creep stresses,” Transactions of the American Society of Mechanical Engineers, vol. 74, no. 5, pp. 765–771, 1952.
- [14] S. S. Manson and A. M. Haferd, “A linear time-temperature relation for extrapolation of creep and stress-rupture data,” tech. rep., 1953.
- [15] B. Wilshire, P. Scharning, and R. Hurst, “A new approach to creep data assessment,” Materials Science and Engineering: A, vol. 510, pp. 3–6, 2009.
- [16] D. R. Eno, G. A. Young, and T.-L. Sham, “A unified view of engineering creep parameters,” in ASME Pressure Vessels and Piping Conference, vol. 48296, pp. 777–792, 2008.



Applied Materials Division
Argonne National Laboratory
9700 South Cass Avenue, Bldg. 208
Argonne, IL 60439

www.anl.gov



Argonne National Laboratory is a U.S. Department of Energy
laboratory managed by UChicago Argonne, LLC